

# Contribution of synchrotron radiation to small-angle X-ray scattering studies in hard condensed matter

Jean-Paul Simon

SIMAP (CNRS-INPG-UJF Grenoble), France. Correspondence e-mail: jean-paul.simon@ltpcm.inpg.fr

Received 16 August 2006  
Accepted 20 December 2006

© 2007 International Union of Crystallography  
Printed in Singapore – all rights reserved

Synchrotron radiation, by virtue of its special beam characteristics (high flux, high brilliance, tuneable wavelength *etc.*), has revived interest in small-angle X-ray scattering (SAXS) for hard condensed matter and materials science. New techniques (ultra SAXS, grazing-incidence SAXS, X-ray photon correlation spectroscopy *etc.*) have been developed and new scientific themes tackled, ranging from metallurgy to nanotechnology.

## 1. Introduction

Formerly, small-angle X-ray scattering (SAXS) studies were used to characterize nano-objects in alloys (Guinier–Preston zones), but they now mainly involve soft condensed matter, a field that will not be discussed here. In hard condensed matter, SAXS has hardly enjoyed the same growth over the last few decades, being confronted by improvements in quantitative microscopy: transmission electron microscopy (TEM) and tomographic atom probe (TAP) analysis for nanoparticles, field-emission-gun TEM for submicrometre-sized particles, scanning tunnelling microscopy (STM) and atomic force microscopy (AFM) for surface nanodots. Although the problem of representative sampling still remains in imaging methods, interest in SAXS has revived mainly by virtue of the specific qualities of synchrotron radiation. A crosscheck with direct-space observations is generally necessary, as previously.

Several beamlines on second- and third-generation synchrotrons are suited – or dedicated – to SAXS experiments. Their specificity is as much conditioned by the source, the optics and the slits (Livet *et al.*, 2003) as the camera design. Although two-dimensional (2D) images are generally employed, allowing anisotropic measurements or improving statistics by azimuthal averaging, detectors remain a key problem. Image plates have read-out times that are too long. Direct illumination charge-coupled devices (CCDs) are reserved for X-ray photon correlation spectroscopy (XPCS) since they are used in photon-counting mode (Livet *et al.*, 2000). The most commonly used cameras are based on a CCD coupled to a phosphor screen by demagnifying fibre optics (coming in various sizes, speeds and signal-to-noise ratios). Finally, the pixel detector developed on the *diffraction et diffusion anormale multilongueur d'onde* (D2AM) beamline at the European Synchrotron Radiation Facility (ESRF; Basolo *et al.*, 2005, 2007) or by Schlepütz *et al.* (2005) for grazing-incidence SAXS (GISAXS) at PSI (Switzerland) will work in a completely parallel counting mode and improve acquisition in all the areas mentioned above.

The scattering vector  $\mathbf{q}$  is defined as the difference between the wave vectors of the incoming beam and the scattered beam. Its modulus  $q$  is equal to  $4\pi \sin(\theta/2)/\lambda$ , where  $\lambda$  is the photon wavelength and  $\theta$  is the angular deviation. If weak diffuse scattering is excluded, the small-angle intensity (in the simple case of precipitates embedded in a matrix) is equal to the product of the contrast between the two phases ( $i = p$  and  $m$  for precipitates and matrix, respectively)

and of the geometrical structure factor  $S_\phi(q)$ , *i.e.* the Fourier transform of pair correlations inside a phase (Patterson function):

$$d\sigma/d\Omega(q, t) = [\rho_p(E, t) - \rho_m(E, t)]^2 S_\phi(q, t). \quad (1)$$

where  $\rho_i$ , the ‘electronic’ density of phase  $i$ , is the sum of the contribution of all elements.  $\rho_i$  may be modified if the photon energy,  $E$ , is close to an absorption edge of one element. This phenomenon is called anomalous small-angle X-ray scattering (ASAXS; see §6). Time-resolved experiments are indicated by the index  $t$  (see §§2 and 3). In case of GISAXS (§4), the scattering angles ( $q \rightarrow q'$ ) have to be corrected for refraction.

As the applications of small-angle scattering (SAS) to materials science have been thoroughly reviewed by Kostorz (1996), Williams *et al.* (1999) and Fratzl (2003), we will focus this paper on the benefit of synchrotron radiation in the various topics listed in Table 1, which outlines the different possibilities. Often more than one quality or technique is combined in a given investigation. Note that brilliance is the ratio of the flux to the ‘emittance’ (focus size and convergence) at the sample position. Experiments are always a compromise between these three extremes: high flux, emittance and brilliance.

In §2, high flux will mainly be illustrated by studies on the weldability of Al alloys. The advantage of hard X-rays is outlined briefly in §3. Discussions of emittance (§4) will concern GISAXS experiments for several studies from superficial dots to layers of nanoporous dielectrics. High brilliance (§5.1) is needed for multiscale samples such as aerogels or surface alteration of glasses. The highest brilliance (§5.2) is mandatory for coherent SAXS, such as for the dynamics of out-of-equilibrium coarsening during phase separation in alloys. Some possibilities of ASAXS will be presented in §6. This review will conclude with a short outlook (§7).

## 2. High-flux experiments for alloy design: exploiting the different synchrotron-radiation SAXS possibilities

Welding of aluminium alloys is increasingly a key joining process in the transportation industry: aluminium alloys based on the Al–Zn–Mg system are suitable for many automotive applications. Generally, in age-hardenable alloys, improved mechanical properties are obtained by homogenization of the solid solution, quenching and aging in a temperature range between 373 and 473 K. At lower temperatures,  $T_{GP}$ , there is precipitation of Guinier–Preston (GP)

**Table 1**  
Synchrotron radiation in small-angle X-ray scattering studies.

Section	Synchrotron radiation	SAXS techniques	Scientific topics
§2	High flux (hard X-rays)	Weak scatterers	<i>In-situ</i> (temperature, chemical reaction <i>etc.</i> )
§3		Time-resolved	Coupled with scattering/diffraction in a different $q$ range
§4	Emittance	$\mu$ SAXS (micro-beam SAXS)	Cartography
		GISAXS	Nanodots, nanoobjects, superficial layers, buried defects
§5	High brilliance to coherence	USAXS (ultra-low- $q$ SAXS)	Sizes overlap with visible light: multiscale scatterers
		XPCS	Dynamics
§6	Tunable wavelength	A(GI)SAXS	Chemically sensitive/partial structure factors

zones, a local enrichment of solutes in the f.c.c. lattice. At higher temperatures ( $\geq 473$  K), a coarse, incoherent precipitation of the stable phase  $\eta$  occurs that no longer contributes to the hardening. High specific mechanical properties are obtained by precipitation of the metastable phase  $\eta'$  with sizes between 50 and 100 Å at  $T_{\eta'}$  (6 h at 373 K + 15 h at 413 K). This  $\eta'$  phase is in an epitaxial relationship with the Al matrix. Its crystallography is close to  $\eta$ , but it is definitely a different phase. As we shall see later, it has a different composition and, during  $\eta'$  reversion,  $\eta$  nucleation takes place independently.

Classical X-rays (8 keV, 1.54 Å) and a  $q$  range  $\sim 0.01$ – $0.3$  Å<sup>-1</sup> could be chosen, but to perform such *ex-situ* measurements in a laboratory would take months (the flux is between  $10^{10}$  and  $10^{11}$  photons s<sup>-1</sup> on the French cooperative research group beamline D2AM on a bending magnet at ESRF, *i.e.* around  $\sim 10^4$  times that of a camera on a rotating anode). The kinetics of time-resolved experiments are often limited by the dead time of the CCD camera and data transfer.  $4 \times 4$  binning decreases the transfer delay from  $\sim 20$  s to less than 2 s.

### 2.1. Cartography

During welding, the base material is modified outside the melting zone owing to the high-temperature cycle experienced in the so-called heat-affected zone (HAZ): as a basic cartograph, Fig. 1 presents a profile, perpendicular to the weld, of the hardness, the radii of the particles and the volume fractions deduced from SAXS in the

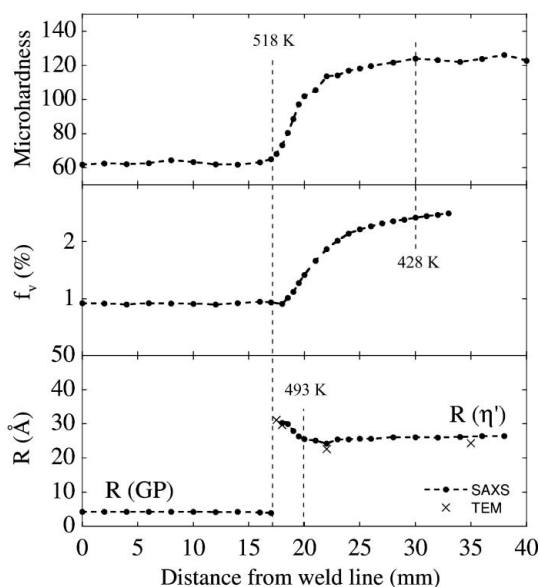


**Figure 1**  
A  $T_{\eta'}$  weld characterized by SAXS (full circles) and by TEM image analysis (crosses): evolution of the microhardness along the heat-affected zone and of the precipitation parameters, volume fraction  $f_v$  and mean particle radii  $R$  at the 'peak' temperatures (from Nicolas & Deschamps, 2004; courtesy TMS).

$T_{\eta'}$  state of the alloy: near the weld the reversion is complete and far from the weld the precipitation is unaffected; in between, *i.e.* in the HAZ, there is a coarse precipitation with a drop in volume fraction as the weld is approached. The thermal cycle – computed or recorded – at all points of the HAZ is characterized by a rapid increase of the temperature up to the 'peak' temperature, followed by the slow cooling stage. In order to disentangle this complex behaviour and to simulate and forecast the precipitation sequence near the weld, the thermodynamics and kinetics of the  $\eta'$  and  $\eta$  phases have first to be specified.

### 2.2. Phase compositions, and complementarities of SAXS, TAP analysis and TEM

It is well known that SAXS alone cannot give the compositions and volume fractions  $f_v$  separately, since they are linked by the 'invariant', the integrated intensity  $Q_0$ :

$$Q_0 = (2\pi^2)^{-1}(\rho_p - \rho_m)^2 f_v (1 - f_v). \quad (2)$$

The volume fraction  $f_v$  should also obey the following relationship for the balance of the elements between the two phases,  $c_{0,i}$  being the global concentrations:

$$f_v = (c_{0,i} - c_{m,i}) / (c_{p,i} - c_{m,i}), \quad i = \text{Al, Mg or Zn}. \quad (3)$$

The electronic contrast between Mg and Al is negligible with respect to that between Zn and Al. We therefore pay attention only to the difference in Zn concentration  $\Delta C_{\text{Zn}}$  in the precipitates and in the matrix. Equations (2) and (3) (Deschamps *et al.*, 2001) are two independent relations between  $f_v$  and  $\Delta C_{\text{Zn}}$  ( $c_{p,\text{Zn}} - c_{m,\text{Zn}}$ ), but are insufficient to solve the problem. Therefore, analysis starts from the overall and matrix concentrations, given by TAP analysis, where the TAP corrections are the most reliable. For acceptable hypotheses, the locus of confidence is diamond-shaped (Fig. 2) and is compatible with TEM and TAP results. The atomic composition of the metastable phase  $\eta'$  is close to  $\text{Zn}_{52}\text{Mg}_{25}\text{Al}_{23}$  (numbers indicate at.%) and that of the stable phase  $\eta$  is  $\text{Zn}_{59}\text{Mg}_{33}\text{Al}_8$ . As already stated, a lot of Al remains in the  $\eta'$  phase. The composition in the  $\eta$  phase is much closer to incoherent bulk  $\text{Zn}_2\text{Mg}$  than that in the  $\eta'$  phase, but Al is still significantly present in small semi-coherent  $\eta$  precipitates.

### 2.3. In-situ anisothermal treatments (time-resolved)

To simulate the temperature cycle in the HAZ, the response of this alloy to thermal ramps from 10 to 300 K min<sup>-1</sup> was investigated by time-resolved SAXS experiments starting from three states:  $T_{\text{GP}}$ ,  $T_{\eta'}$  and  $T_{\eta}$  (Deschamps, Nicolas *et al.*, 2005). In the first case, the GP zones completely dissolve; afterwards, the stable  $\eta$  phase precipitates and finally dissolves (Figs. 3a, b): we point out that the second  $\eta$  precipitation does not occur when the heating rate is too high;  $\eta$  nucleation is skipped (Fig. 3a). Starting from  $\eta'$  (Fig. 3b), there are two dissolution states, also shown by differential scanning calorimetry measurements, which are superimposed: the first corresponds to  $\eta'$

dissolution, together with  $\eta$  nucleation and growth and, finally, starting from  $\eta$ , only its dissolution is observed (Fig. 3b). Above 553 K, the dissolution behaviour is independent of the history of the samples: at these temperatures the volume fraction follows that of the equilibrium phase diagram.

To understand these reversion stages better, the samples were rapidly heated, followed by an isothermal treatment (Fig. 4). The evolution of the precipitation state can be divided into two stages:

(1) fast dissolution down to a minimum volume fraction, with no significant change of the mean particle radius,  $R$ ;

(2) subsequent increase of  $f_v$  and  $R$  (which will be identified as the 'coarsening stage').

The stability of a precipitate of a given size in the solid solution, outlined by Gibbs Thomson, is dictated by the respective values of the equilibrium solute concentration at the precipitate/matrix interface and the average solute content in the matrix: no nucleation is considered. One generally refers to the critical radius  $R^*$ , where

$$R^* = 2\gamma v_{at}/kT \ln(X/X_{eq}), \quad (4)$$

where  $\gamma$  is the interface energy,  $k$  is the Boltzmann constant and  $X$  stands for concentration. The precipitates with  $R < R^*$  shrink while those with  $R > R^*$  increase in size. When the thermodynamics of the system are known, the measurement of coarsening kinetics allows an

independent determination of  $\gamma$  and of the diffusion (for Cu-Fe see Deschamps, Genevois *et al.*, 2005). In the Al-Zn-Mg alloy, the existence of two solute elements complicates the situation. The chosen modelling approach is the so-called class model, first introduced by Wagner & Kampmann (1991). Its basic principle is to discretize the precipitate size distribution and to have a master equation for the evolution of each size class. The master equation is the Zener growth/dissolution equation, where concentrations and the atomic diffusions are those of the limiting diffusing solute, namely Mg. Thermodynamics, approximated by a regular solution, gives the Gibbs Thomson effect.

Finally, the concentrations are calculated by considering the stoichiometry of the precipitates ( $Zn_2Mg$ ), which imposes a ratio of 2 on the solute flux of Zn and Mg. The results of this model, calibrated on the experimental precipitation kinetics, are shown by continuous lines (Figs. 4a, b): at the beginning of the thermal ramp, the critical radius  $R^*$  (Fig. 4c) is much larger than the average radius, which entails a destabilization of the precipitate size distribution and rapid dissolution. The radius  $R^*$  drops due to this rapid enrichment of the solute concentration and the stability of the surviving precipitates increases. When  $R^*$  becomes smaller than the average radius  $R_{mean}$ , coarsening begins and  $R^*$  remains slightly smaller than  $R_{mean}$ .

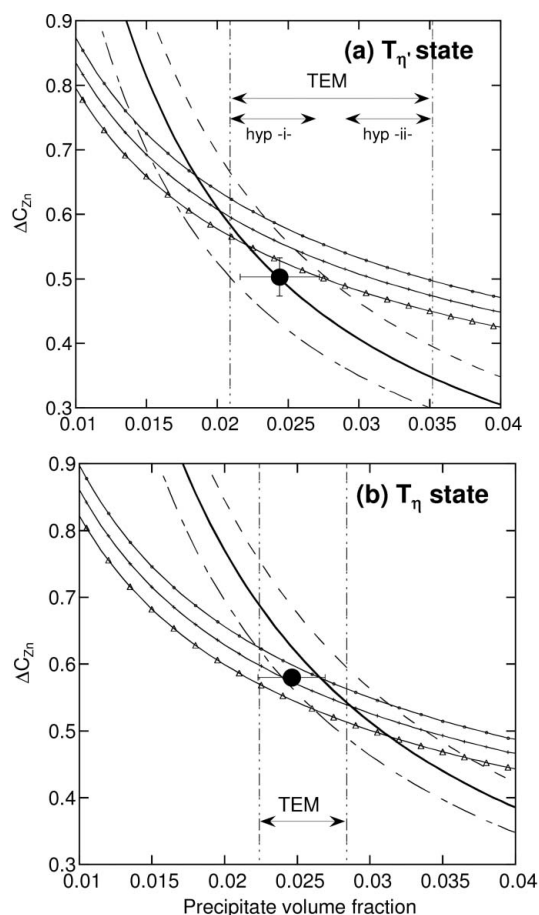


**Figure 2** Relationship between the Zn contrast (precipitate composition – matrix composition) and the precipitate volume fraction for the  $T_{\eta}$  state and the  $T_{\eta}$  state (a and b, respectively). Slightly inclined curves correspond to equation (2) with different hypotheses on Al composition in the precipitates. Steep curves correspond to equation (3) for different hypotheses in the confidence range for the overall and matrix Zn contents. TEM and TAP (filled circles) evaluations are also reported (M. Dumont *et al.*, 2005; courtesy Elsevier).

### 3. Hard X-ray SAXS

Hard X-rays are necessary in the case of a strongly absorbing sample or sample environment: they have been used for *in-situ* high-pressure measurements of supercritical fluids (Testemale *et al.*, 2005) and the characterization of the glass transition of vitreous silica by

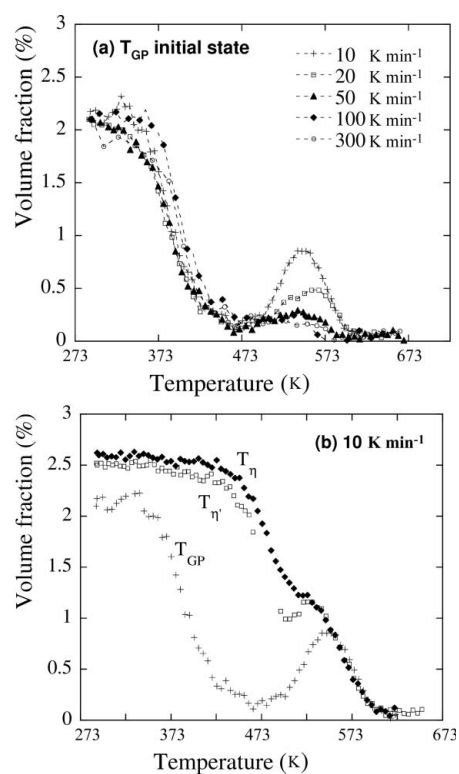


**Figure 3** (a) Evolution of the volume fraction for the indicated heating rates during continuous heating experiments on the Al-Zn-Mg alloy, initially in the  $T_{GP}$  state. (b) Reversion during 10 K min<sup>-1</sup> heating of three initial states,  $T_{GP}$ ,  $T_{\eta}$  and  $T_{\eta}$  (Deschamps, Genevois *et al.*, 2005; courtesy Taylor & Francis).

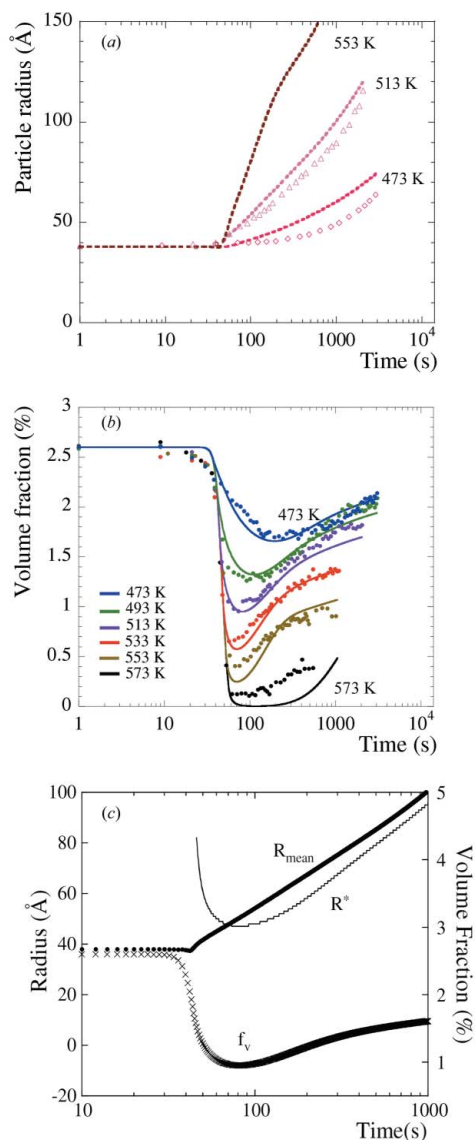


**Figure 4**  
 (a), (b) Comparison between experimental results and model predictions for the Al-Zn-Mg alloy, initially in the  $T_\eta$  state, subjected to isothermal reversion treatments at temperatures between 473 and 573 K. (c) Focus on the model prediction of the evolution of volume fraction, critical radius and average radii during the 413 K treatment (Deschamps, Genevois *et al.*, 2005; courtesy Taylor & Francis).

temperature-scanning SAXS (Levelut *et al.*, 2007). It should in principle be possible to study bulk crystalline samples as with neutrons, but, since Bragg diffraction cannot be avoided and since the X-ray–matter interaction is much stronger than that between neutrons and matter, multiple scattering often appears. For instance, in a study of NbC in Fe, multiple diffraction strikes spoiled the SAXS images and the investigation had to be carried out using neutrons (Perrard *et al.*, 2006).

**4. Emittance-dependent experiments: grazing-incidence SAXS**

During the last decade, the GISAXS technique has developed as fast as nanotechnology. Synchrotron radiation is mandatory since the grazing angle is a few tenths of a degree (therefore the footprint of a

0.1 mm high X-ray beam on the sample is a few centimetres long). In general, a large part of the incident beam is of no use and, since the probed volume is tiny, signals are weak. Finally, if the sizes can be determined, the integrated intensities (*i.e.* the volume fractions) are out of reach. Despite these difficulties, the use of GISAXS is expanding rapidly for the characterization of superficial dots (a), buried implanted defects (bubbles) (b), co-deposited materials (c) and nanoporous dielectrics (d).

(a) The state of the art was demonstrated with *in-situ* GISAXS characterization during molecular beam epitaxy deposition on monocrystalline substrates (Renaud *et al.*, 2003; Fig. 5). Several systems were studied: metallic and/or magnetic dots on metals, on oxides or on van der Waals surfaces ( $WS_e_2$ ). The shape, sizes, and surface repartition of the islands and their distributions were simulated in the framework of the distorted-wave Born approximation by the well known *IsGISAXS* analysis program (Lazzari, 2002).

Nanomeric Ge–Si islands in a regular array are good candidates for quantum dots: the confinement of the electron wavefunction to dimensions of the order of 100–1000 Å, smaller than the electron mean path, drastically changes both the energy levels and the density of states. Schmidbauer *et al.* (2005a,b) studied the shape of Ge–Si islands grown by epitaxy on an Si substrate and the associated strains. Grazing-incidence wide-angle X-ray scattering (GIWAXS) was also measured near the Bragg peak to take into account the strains. The distribution of this intensity strongly depends on the grazing angle: the authors found it necessary to use at least 5 GISAXS and 9 GIWAXS scattering images at different angles to achieve the analysis. Vartanyants *et al.* (2005) also studied Ge–Si auto-organized quantum dots by semi-coherent GISAXS (*cf.* §5.2): the deduced

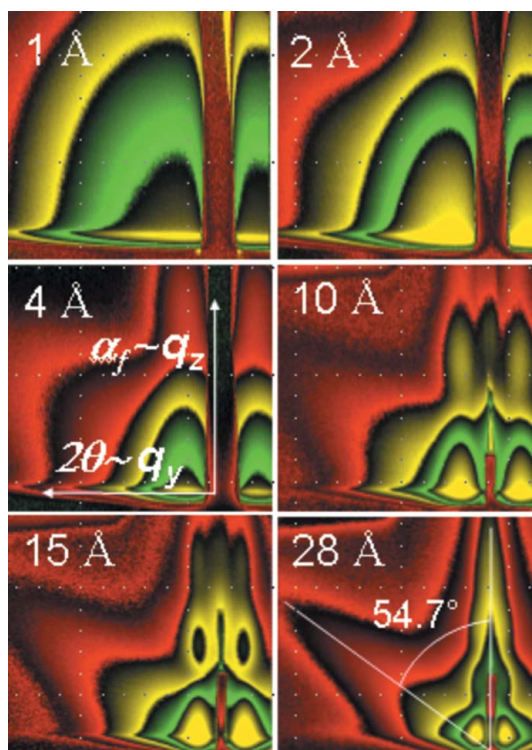


**Figure 5**  
*In-situ* GISAXS measurements during Pd deposition on MgO (001) at 650 K for different thicknesses, with the incident beam along the MgO [110] direction. The vertical direction is perpendicular to the sample surface and the horizontal direction is parallel. Data for other beam directions show that the islands were truncated octahedrons. From the simulations, their spacing, lateral size, height and polydispersity were determined (Renaud *et al.*, 2003).

periodicity, size and shape of the Ge–Si islands was found to be in agreement with the AFM data.

(b) The size distribution, shape distribution and depth profile of defects induced by He and Ne implantation in Si has been extracted from GISAXS data obtained with different grazing incidences (Babonneau *et al.*, 2007). 10 keV hard photons were used in order to increase the probed depth down to  $\sim 1$   $\mu\text{m}$ .

(c) Oxide–metal layers, co-deposited for their optical properties:

(i) Ceramic metal (cermet) thin films are good radiation absorbers in the visible-light or near-infrared regions of the solar spectrum: when metallic clusters are confined in an insulator matrix, strong absorption appears near the UV-VIS region due to surface plasmon resonance. To improve optical tunability, several studies aimed at understanding the optical properties from the structural analysis have been carried out: co-sputtered Au in  $\text{Al}_2\text{O}_3$  was studied by Hazra *et al.* (2004) and Ag in  $\text{Si}_3\text{N}_4$  was studied by Camelio *et al.* (2003, 2005).

(ii) Co-, Fe-, Ni-, CoPt- and FePt-based nanocomposite materials in which nanoparticles are encapsulated in a nonmagnetic matrix (*e.g.* C, BN) have unique magnetic, electronic, optical and transport properties. Boron nitride, which crystallizes in a structure similar to graphite but is a good electrical insulator, may have significant advantages for controlling spin-dependent tunnelling between nanoparticles. Ion-sputtering co-deposition of Fe and BN was assisted by a second beam of reactive (nitrogen) or inert (Ne, Ar, Kr) ions (Babonneau *et al.*, 2005). With inert-gas-assisted films, amorphous  $\text{Fe}_2\text{B}$  nano-columns have been synthesized in self-organized arrays. The best result was obtained with 50 eV Ar-assisted films: among inert gases, argon minimizes the energy transfer to the surface atoms.

(d) Microelectronics research and development try to improve the functionality and speed of integrated circuits in smaller packages. One of the key problems at present is the crosstalk between wires through the dielectric barrier. The high-frequency capacitance is compared to that of a vacuum by the ratio  $k$  ( $>1$ ). Introduction of pores (ultra-low- $k$  materials) decreases  $k$  without damaging the mechanical properties if the pores are of nanometre size and are homogeneously distributed. As emphasized by Lee *et al.* (2005) and by Simon *et al.* (2007), GISAXS gives supplementary information on the shape of pores and their spatial pattern (anisotropy, spatial ordering *etc.*) to those given by X-ray reflectivity and ellipsometry porosimetry (volume fraction of pores and pore sizes).

## 5. High brilliance

High brilliance is a combination of a small focus size and a small divergence, as needed in ultra SAXS (USAXS) and for coherent beams in X-ray photon correlation spectroscopy (XPCS).

### 5.1. Ultra SAXS and multiscale SAXS scatterers

Both the size of the focus on the detector and the convergence have to be small in order to reach a very low  $q$  cutoff, close to that of neutrons. On the other hand, if a large  $q$  range is needed, as for instance in aerogels, which are multiscale structures, detectors do not have a sufficient dynamic range and one has to perform the measurements at several sample-to-detector distances. Carbon aerogels characterized by high specific surfaces (above  $1000 \text{ m}^2 \text{ g}^{-1}$ ) and high electrical conductivity are particularly suitable as electro-catalyst supports. Berton-Fabry *et al.* (2004) prepared them by several-step sol–gel reactions (Fig. 6).

This unexpected anisotropy, attributed to strains induced during preparation near the critical gelation limit, has been detected using a two-dimensional detector and a standard Guinier camera. In

contrast, a measurement with a Bonse–Hart camera would probably have missed this feature.

Surface alteration of glasses is very important in preventing nuclear-waste elements from dissolving in hot water. The precursors are nanoporous micrometre-size powders: the interstitial solution and the filling of the internal pores need to be determined. It is important to work *in situ* to avoid corruption of the results by capillary forces. Nevertheless, the thickness of the layer between grains is unknown. This SAXS problem can be overcome if the measured  $q$  range is sufficient (Spalla *et al.*, 2003): two Porod regimes emerge, at low  $q$  due to the intergranular medium, and at high  $q$  due to the inner pores. Equations for the three possibilities, liquid everywhere, only in the pores or only in the interstices, were established. Their study concluded that there is an altered layer with water everywhere and was able to determine the composition of the remaining skeleton.

### 5.2. X-ray photon correlation spectroscopy

When the coherence of the X-ray beam becomes significant, *i.e.* when the product of the beam divergence and the beam size is smaller than the photon wavelength, speckles appear in the patterns. This interference pattern is in direct relation to the position of the individual scattering objects. The phase is in principle recovered.

Nevertheless, even in static measurements, researchers struggle to have univocal correspondence between coherent USAXS images and ‘object’ reconstruction: they call it ‘three-dimensional X-ray diffraction microscopy’ (Beetz *et al.*, 2005) and it is used mainly for biological applications.

Several non-trivial kinetics experiments have been performed for the study of equilibrium or non-equilibrium phenomena. In the case of equilibrium phenomena, the calculation of the autocorrelation suffices, since only the time interval between measurements is significant. In the case of non-equilibrium phenomena, discussed hereafter, a two-time correlation function is needed: the phase separation during the coarsening regime is a generic non-equilibrium phenomenon of non-conservative phase transitions. Several isothermal kinetics have been studied on a sodium borosilicate glass (Malik *et al.*, 1998), and on Al–Li (Livet *et al.*, 2001), Al–Zn and Al–Ag alloys (Stadler *et al.*, 2004).

These systems were chosen because the phase separation occurs on the same ‘lattice’, precipitates remaining spherical during their growth due to the small misfit. The ‘average’ kinetic scaling  $\langle I(q, t) \rangle$  obeys the well known Lifschitz–Slyosov–Wagner (LSW) (Lifschitz & Slyosov, 1961; Wagner, 1961) coarsening, but the dynamic scaling is an unsolved problem.

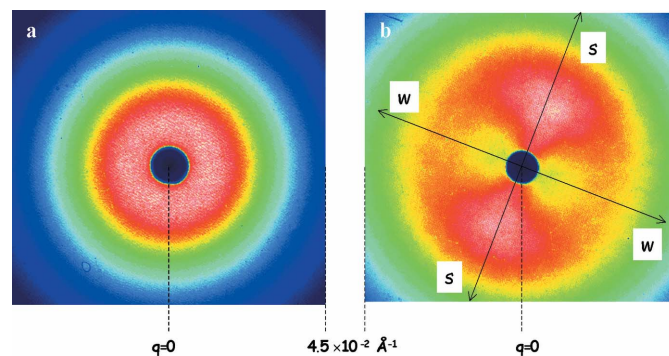


**Figure 6**  
SAXS patterns of C aerogels formed by sol–gel catalysis-enhanced reaction, (a) in aqueous solution, (b) in acetone. *s* (strong) and *w* (weak) indicate the anisotropy directions (Berton-Fabry *et al.*, 2004; courtesy Elsevier).

Typical behaviour of the time evolution of the normalized intensity fluctuations  $N$  for several pixels at the same  $q$  is shown in Fig. 7 for Al–Li: fluctuations slow down with time. The time dependence of the speckle pattern allows the long-term correlations to be determined, defining the two-time correlation function as the average of the product of  $N$  at  $t_1$  and  $t_2$ :

$$C(q, t_1, t_2) = \langle N(q, t_1)N(q, t_2) \rangle. \quad (5)$$

A proposed functional form associated with a moving interface model provides an accurate estimation of the characteristic correlation time  $\tau$ . Finally, the correlation times were scaled for all  $q$  values, the scaling factor being the time  $t_{\max}$  where the maximum of the hump-shaped intensity reaches a given  $q$  value. All data collapse to a single curve (Fig. 8).

These results agree quite well with the theory of Brown *et al.* (1999). Two power laws emerge:

(1) Early on, the correlation grows linearly with time and  $\tau$  is of the same order of magnitude as the overall aging time. The peak position comes from the relative position of the larger precipitates. An evaporation–condensation mechanism is found. The relative position of the larger precipitates does not change, whereas small precipitates evaporate as their atoms condense on larger ones.

(2) At later times, the persistence time  $\tau$  of the speckles is the longest for the smallest  $q$  values, *i.e.* for the largest sizes. In scaled parameters, this corresponds to the upper part of the curve of Fig. 8 which follows a  $t^{2/3}$  behaviour. This is related to the asymptotic part of the intensity and reflects interface fluctuations.

In the case of Al–Zn and Al–Ag, Stadler *et al.* (2004) discuss their results from another point of view, based on the Monte Carlo simulations of Weinkamer & Fratzl (2003): in metals and alloys, solid-state diffusion occurs by vacancy jumps in which local concentrations as well as jump frequencies differ if the jumps involve a solute atom or a solvent atom. This gives two predominant coarsening mechanisms: if vacancies are found preferentially in the matrix, coarsening will

proceed *via* diffusion of atoms from smaller precipitates to larger ones, the classical evaporation–condensation LSW mechanism. On the other hand, if vacancies are localized preferentially in the precipitates or at their interfaces, the barycentre of the precipitates moves and, when they touch one another, they coagulate. Through a Fourier analysis, the conclusion was that coagulation prevails in Al–Zn and, on the contrary, evaporation–condensation dominates in Al–Ag.

## 6. ASAXS results

Two reviews (Simon & Lyon, 1994; Goerigk *et al.*, 2003) have covered the different possibilities of this element-specific technique. Most applications need only differential ASAXS, which is fairly easy to handle. In contrast, measurements coupling quantitative anomalous scattering at small angles and at large angles gave the most detailed description of the nanostructure in selected ternary alloys.

### 6.1. Contrast enhancement, separation of different kinds of scattering objects, composition of phases

As a first example, the contrast  $(f_{\text{Cu}} - f_{\text{Fe}})^2$  in the SAXS study of precipitation of Cu particles in an Fe matrix is increased by a factor of 8 by using a photon energy of 7106 eV, just below the Fe edge (7112 eV) (Deschamps, Genevois *et al.*, 2005). From an *in-situ* ASAXS study, by means of isothermal aging in the coarsening regime, the diffusion constant and the interfacial energy were determined.

Differential ASAXS allows identification of ‘objects’ containing the anomalous element in the presence of others: any signal independent of the photon energy can be considered as background. For example, control of the primary crystallization of f.c.c. Ni particles in an amorphous Ni<sub>83</sub>P<sub>17</sub> (at.%) amorphous alloy (Tatchev *et al.*, 2005) is important to optimize thin-film magnetic memories. Anomalous SAXS was recorded at several photon energies near the Ni *K* edge energy: at small  $q$  values ( $q < 0.06 \text{ \AA}^{-1}$ ), the anomalous signal varies as the square of the mean electronic density; it is attributed to the

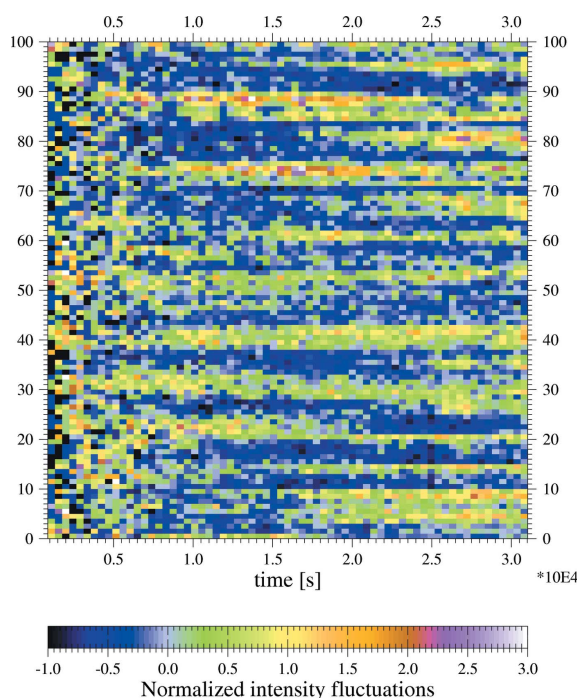


**Figure 7** Evolution of intensity fluctuations for some pixels at  $q = 0.0117 \text{ \AA}^{-1}$  (from Livet *et al.*, 2001; courtesy American Physical Society).

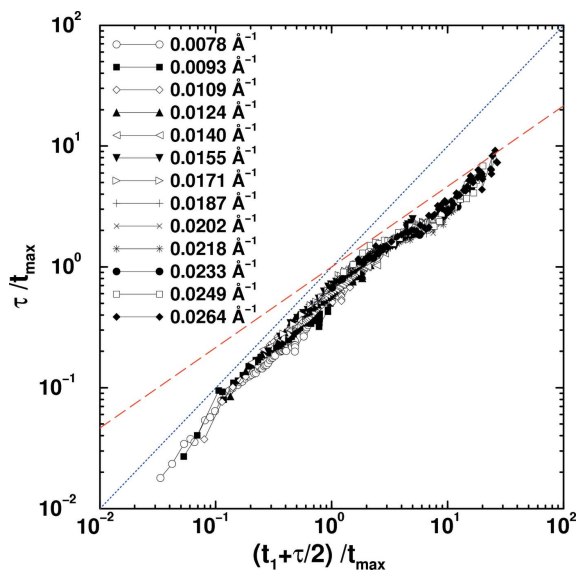


**Figure 8** Scaled fitted correlation times for all values. The dotted line has a slope of 1 and the dashed line has a slope of 2/3 (Livet *et al.*, 2001; courtesy American Physical Society).

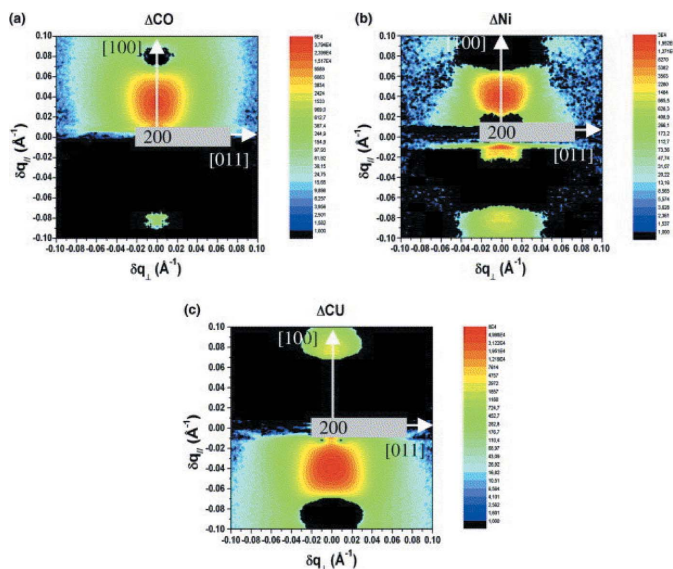


**Figure 9** Two-dimensional maps showing  $\Delta I$  versus  $\delta q$  [equation (6)] in the [100] direction of the precipitate alignment and in the [011] orthogonal direction for (a) the Co, (b) the Ni and (c) the Cu partial displacements for a  $\text{Cu}_{70}\text{Ni}_{23}\text{Co}_7$  (at.%) single crystal aged for 12 h at 823 K (from Guillon *et al.*, 2005; courtesy Elsevier).

scattering of large surface defects. The largest anomalous variation occurs near  $0.12 \text{ \AA}^{-1}$ , but its amplitude varies with the scattering vector: the pattern differs from the ‘two-phase model’ where the matrix is homogeneous and particles also have a unique composition. A size distribution of Ni–P precipitates was therefore introduced, where the P content  $c_p$  varies with the size: as the radii of the particles increases from 7 to about  $30 \text{ \AA}$ ,  $c_p$  decreases from 14% to ~2% and remains smaller than 2% for larger particles.

**6.2. Coupling ASAXS/anomalous wide-angle X-ray scattering (AWAXS)**

**6.2.1. Precipitation patterns and displacements.** The displacements are known to be the main origin of the shape of the precipitates and of their spatial pattern: during their growth, they change from spheres with an ill ordered pattern to faceted particles arranged in a regular pattern. The theoretical approaches are recent (reviewed by Fratzl *et al.*, 1999): few experiments exist on single crystals.  $\text{Cu}_{70}\text{Ni}_{23}\text{Co}_7$  (at.%) (Guillon *et al.*, 2005; Lyon *et al.*, 2005) undergoes phase separation into an Ni–Co-rich phase and a Cu-rich phase: since the bulk parameter of the Ni–Co phase is smaller than that of the Cu phase, there are lattice strains in both phases. The anisotropy of the lattice constants induces a pile-up along the weak  $\langle 100 \rangle$  directions. The original method for extracting displacements is based on the symmetry and periodicity of the successive terms of the expansion of the scattering equation (Lyon *et al.*, 2000):

**Table 2** Structural parameters during ordering and precipitation in a model superalloy Ni–Cr–Al aged at 873 K.

Aging time (h)	ASAXS Radius (Å)	ASAXS $C_{Al, p}$	ASAXS $f_v$	XRD Radius (Å)	AXRD $S_{Cr}^\dagger$	AXRD (5.8 keV) Integrated intensities
0.33	10.0	0.12	(0.11)	—	—	—
1	11.3	0.14	0.08	12.4	0.22	6.8
2	14.3	0.17	0.09	13.3	0.18	7.1
4	16.35	0.185	0.106	16	0.17	6.3
8	19.0	0.20	0.116	19.6	0.16	6.3

<sup>†</sup> Order parameter.

$$\Delta I(\Delta q_B) = I(\Delta q_{B+}) - I(\Delta q_{B-}). \tag{6}$$

This antisymmetric part of the diffuse scattering  $\Delta I$  is proportional up to the third order to the Fourier transform of the displacement field. The 2D images near the 200 Bragg peak in the (001) zone axis present two lobes in the [100] direction; the difference  $\Delta I(\Delta q_B)$  is positive, then negative, and finally tends towards zero. Its Fourier transform indicates a contraction of the matrix lattice and a dilatation of the precipitates. This explains the regularly spaced pattern of precipitates. The repulsion between precipitates at short distance, followed by an attraction, can also be described by the ‘partial displacement factors’ (PDFs) (Fig. 9), the equivalent of the ‘partial structure factors’ (PSFs) for atom segregation. Co and Ni are in the same phase, which tends to contract the overall lattice, and Cu has the opposite effect, leading to a PDF of opposite sign. The third element,  $X = \text{Co}$  or  $\text{Fe}$ , in Cu–Ni-based alloys modifies the Ni–X-rich phase morphology: in Cu–Ni–Co spherical precipitates slowly evolve towards ellipsoids, while in Cu–Ni–Fe they rapidly form platelets (TEM images exhibit a tweed contrast). This morphology difference is due to a different balance between surface and strain energies, but it only weakly influences the deformation field, which is essentially located along the pile-up direction.

**6.2.2. Phase separation and ordering in a model Ni–Cr–Al superalloy by ASAXS and anomalous X-ray diffraction.** The question to be answered in this study (Bley *et al.*, 1997; Delheusy, Bley, Gaspard, Livet, Okuda & Simon, unpublished) was: which type of fluctuations (order fluctuations or composition fluctuations) occurs first?

The SAXS profiles during isothermal annealing present maxima that increase and shift towards low  $q$  values (Fig. 10; Table 2).

This interference ring gives the mean distance between the precipitates, the radius is determined by the maximum of  $Iq^4$  plots and finally the measure of the integrated intensity couples the volume fractions and compositions through equation (2).

Numerous energies near both the Cr and Ni edges were used in the ASAXS data acquisition (Fig. 11a) and allow the calculation of the PSF that gives the most complete structural information available with elastic scattering. The main difficulty arises from the solution of an ill-conditioned system of linear equations (small contrast variations) with the possibility of over-sampling (Lyon, 1993).

The resulting PSFs (Fig. 11b) are compatible with a two-phase pattern, without any segregation of Ni, but a progressive Al enrichment in the precipitates and a corresponding ejection of Cr. The whole kinetics follow a  $t^{0.25}$  law, differing from a standard nucleation, growth and coarsening process.

The 100 superstructure lines (Fig. 12a) were recorded by powder diffraction at different energies. From their width, the domain size can be deduced using the Scherrer relation. The size of these domains is almost the same as that measured by SAXS: precipitates and ordered domains correspond (Table 2).

The partial-long-range-order parameters can be deduced from the intensity variation with the photon wavelength (Marty *et al.*, 1990)

(Fig. 12b): precipitate ordering is complete from the earliest state studied. The decrease of the Cr order parameter to the benefit of Al

order parameter (Table 2) means that  $Ni_3(Al_xCr_{1-x})$  precipitates with an  $L1_2$  structure absorb Al from the matrix and reject Cr during their growth. This is consistent with the fact that ordering may be much faster than phase separation, since it needs an exchange only between neighbouring atoms, while precipitation needs long-range diffusion.

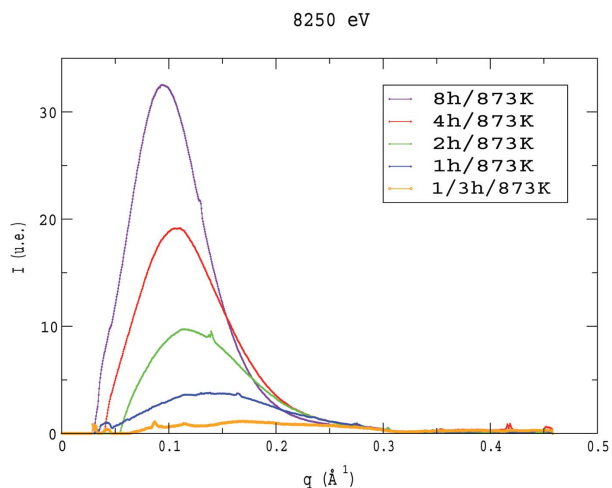


**Figure 10**  
SAXS profile at 8250 eV of a  $Ni_{77}Cr_{17.5}Al_{5.5}$  (at.%) alloy aged at 873 K.

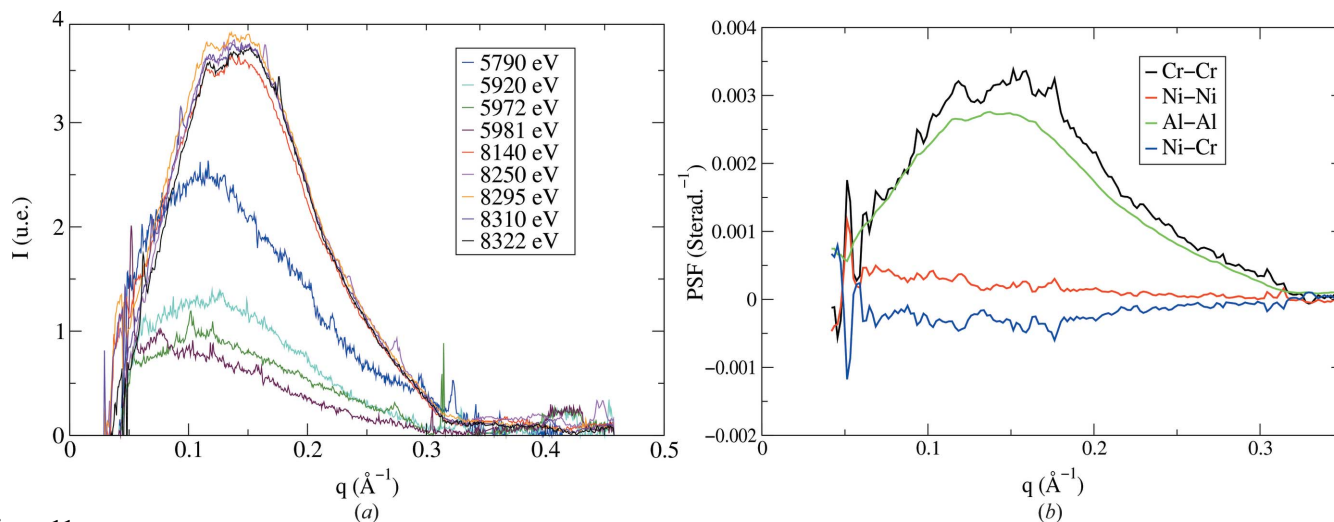


**Figure 11**  
(a) ASAXS profiles for the aging for 1 h at 873 K. Note that the shapes are identical and that the profiles near the Ni edge (8333 eV) superimpose. (b) Corresponding PSFs. The homo-atomic PSFs are positive, as they should be.

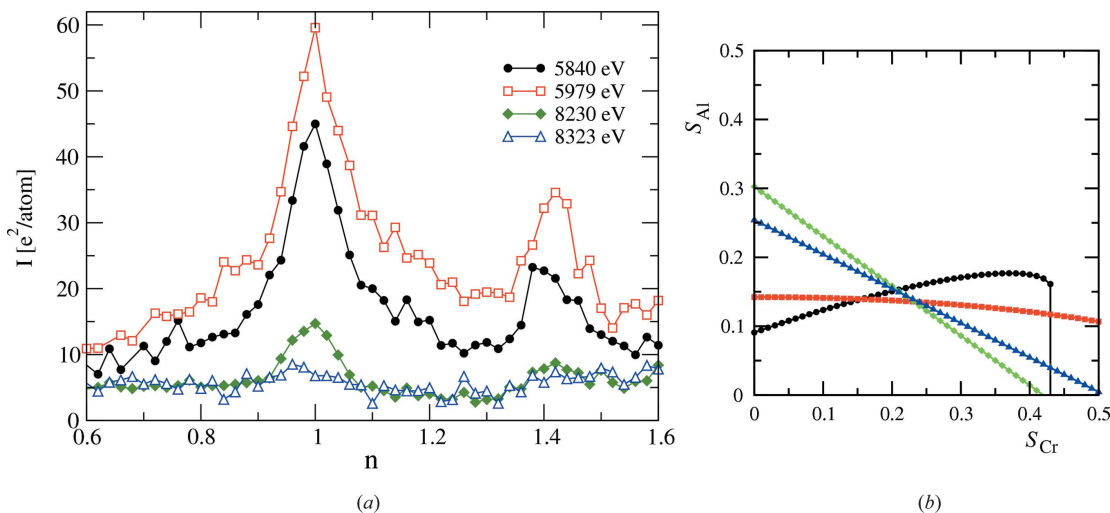


**Figure 12**  
(a) Superstructure profiles for 100 (at  $n = 1$ ) and 110 (at  $n = 2^{1/2}$ ) and (b) compatibility graphs in order-parameter space for aging for 1 h at 873 K.

### 7. Outlook

Synchrotron radiation has already resulted in a considerable boosting of and diversification in SAXS experiments: SAXS already overlaps with visible-light scattering and micrometre-sized beams have begun to be characterization tools for nanotechnology. The race towards rapid kinetics is also a current challenge. New SAXS cameras will soon be operational on third-generation synchrotron-radiation facilities such as Soleil (France) or Diamond (United Kingdom). Upgrading of second-generation synchrotrons is also scheduled: the major goal is improvement of brilliance, more precisely micrometre-sized highly parallel beams. In all fields, *i.e. in situ* with specially designed sample environments, cartography, grazing-incidence SAXS, multiscale scattering and X-ray photon correlation microscopy, new opportunities will appear. Several techniques combined in

the same experiment will become standard, almost the rule. Concerning anomalous SAXS, a gain in brilliance is not the key problem: the monochromator bandwidth is already smaller than the edge width. Stability is essential: machine and optics stabilities are already excellent, but unknown systematic errors may subsist. We also expect that giant magnetic scattering, a resonance near the  $L$  edges in transition metals or near  $M$  edges in heavy elements, will develop, allowing comparison between magnetic domains and chemical domains (Kortright *et al.*, 2005; Fullerton *et al.*, 2003). Finally, since many of the difficult problems in materials and hard condensed matter sciences will never be solved by one experimental technique alone, the micrometre-sized spatial resolution of future SAXS synchrotron beamlines, comparable to the definition of light microscopes or of scanning electron microscopes, will allow outstanding combined experiments.

The author is indebted to F. Bley, A. Deschamps, M. Dumont-Nicolas, F. Livet, S. Berthon-Fabry, G. Renaud and I. Guillon for permission to reproduce Figs. 1 to 9. We thank F. Ehrburger-Dolle, E. Geissler, O. Lyon and M. Maret for their suggestions on the manuscript.

## References

- Babonneau, D., Pailloux, F., Eymery, J. P., Denanot, M. F., Guérin, P., Fonda, E. & Lyon, O. (2005). *Phys. Rev. B*, **71**, 035430(1–13).
- Babonneau, D., Peripolli, S., Beaufort, M.-F., Barbort, J.-F. & Simon, J.-P. (2007). *J. Appl. Cryst.* **40**, s350–s354.
- Basolo, S., Bélar, J.-F., Boudet, N., Breugnon, P., Caillot, B., Clemens, J.-C., Delpierre, P., Dinkespiler, B., Hustache, S., Koudobile, I., Meesen, C., Menouni, M., Mouget, C., Palancher, H., Pangaud, P., Potheau, R. & Vigeolas, E. (2007). *J. Synchrotron Rad.* **14**, 151–157.
- Basolo, S., Bélar, J. F., Boudet, N., Breugnon, P., Caillot, B., Clemens, J. C., Delpierre, P., Dinkespiler, B., Koudobile, I., Meesen, C., Menouni, M., Mouget, C., Pangaud, P., Potheau, R. & Vigeolas, E. (2005) *IEEE Trans. Nucl. Sci.* **52**, 1994–1998.
- Beetz, T., Howells, M. R., Jacobson, C., Kao, C.-C., Kirz, J., Lima, E., Menten, T. O., Miao, H., Sanchez-Hanke, C., Sayre, D. & Shapiro, D. (2005). *Nucl. Instrum. Methods Phys. Res.* **A545**, 459–468.
- Berton-Fabry, S., Langohr, D., Achard, P., Charrier, D., Djurado, D. & Ehrburger-Dolle, F. (2004). *J. Non-Cryst. Solids*, **350**, 136–144.
- Bley, F., Livet, F., Okuda, H. & Simon, J. P. (1997). *J. Appl. Cryst.* **30**, 914–917.
- Brown, G., Rikvold, P. A., Sutton, M. & Grant, M. (1999). *Phys. Rev. E*, **60**, 5151–5162.
- Brumberger, H., Hagrman, D., Goodisman, J. & Finkelstein, K. D. (2005). *J. Appl. Cryst.* **38**, 324–332.
- Camelio, S., Babonneau, D., Girardeau, T., Toudert, J., Lignou, F., Denanot, M.-F., Maître, N., Barranco, A. & Guérin, P. (2003). *Appl. Opt.* **42**, 674–681.
- Camelio, S., Toudert, J., Babonneau, D. & Girardeau, T. (2005). *Appl. Phys. E*, **80**, 89–96.
- Deschamps, A., Bigot, A., Livet, F., Auger, P., Bréchet, Y. & Blavette, D. (2001). *Philos. Mag.* **81**, 2391–2414.
- Deschamps, A., Genevois, C., Nicolas, M., Perrard, F. & Bley, F. (2005). *Philos. Mag.* **85**, 3091–3112.
- Deschamps, A., Nicolas, M., Perrard, F. & Bley, F. (2005) *Solid-to-Solid Phase Transformations in Inorganic Materials*, Vol. 1, edited by J. M. Howe, D. E. Laughlin, J. K. Lee, U. Dahmen & W. A. Soffa, pp. 263–278. Warrendale, PA: TMS.
- Dumont, M., Lefebvre, W., Doisneau-Cottignies, B. & Deschamps, A. (2005). *Acta Mater.* **53**, 2881–2892.
- Fratzl, P. (2003). *J. Appl. Cryst.* **36**, 397–404.
- Fratzl, P., Penrose, O. & Lebowitz, J. L. (1999). *J. Stat. Phys.* **95**, 1429–1503.
- Fullerton, E. E., Hellwig, O., Takano, K. & Kortright, J. B. (2003). *Nucl. Instrum. Methods Phys. Res.* **B200**, 202–209.
- Goerigk, G., Haubold, H.-G., Lyon, O. & Simon, J.-P. (2003). *J. Appl. Cryst.* **36**, 425–429.
- Guillon, I., Servant, C. & Lyon, O. (2005). *Acta Mater.* **53**, 2469–2483.
- Hazra, S., Gibaud, A. & Sella, C. (2004). *Appl. Phys. Lett.* **85**, 395–397.
- Kortright, J. B., Hellwig, O., Chesnel, K., Sun, S. & Fullerton, E. E. (2005). *Phys. Rev. B*, **71**, 012402(1–4).
- Kostorz, G. (1996). *X-ray and Neutron Scattering in Physical Metallurgy*, 4th ed., edited by R. W. Cahn & P. Haasen, pp. 1115–1199. Amsterdam: North Holland.
- Lazzari, R. (2002). *J. Appl. Cryst.* **35**, 406–421.
- Lee, B., Park, Y.-H., Hwang, Y.-T., Oh, W., Yoon, J. & Ree, M. (2005). *Nature Mater.* **4**, 147–150.
- Levelut, C., Le Parc, R., Faivre, A., Bruning, R., Champagnon, B., Martinez, V., Simon, J.-P., Bley, F. & Hazemann, J.-L. (2007). *J. Appl. Cryst.* **40**, s512–s516.
- Levelut, C., Faivre, A., Le Parc, R., Champagnon, B., Hazemann, J. L. & Simon J. P. (2005). *Phys. Rev. B*, **72**, 224201 (1–11).
- Lifschitz, M. & Slyosov, V. V. (1961). *J. Phys. Chem. Solids*, **19**, 35–50.
- Livet, F., Bley, F., Caudron, R., Geissler, E., Abernathy, D., Detlefs, C., Grübel, G. & Sutton, M. (2001). *Phys. Rev. E*, **63**, 036108(1–7).
- Livet, F., Bley, F., Caudron, R., Geissler, E., Abernathy, D., Grübel, G., Mochrie, S. G. J., Sutton, M. & Mainville, J. (2000) *Nucl. Instrum. Methods A*, **451**, 596–609.
- Livet, F., Bley, F., Ehrburger-Dolle, F., Geissler, E., Le-Bolloc'h, D. & Schulli, T. (2003). *J. Appl. Cryst.* **36**, 774–777.
- Lyon, O. (1993). *Methods in the Determination of Partial Structure Factors*, edited by J. B. Suck, P. Chieux, D. Raoux & C. Riekel, pp. 142–150. London: World Scientific.
- Lyon, O., Guillon, I., Servant, C. & Simon, J. P. (2005). *J. Appl. Cryst.* **38**, 476–487.
- Lyon, O., Servant, C. & Simon, J. P. (2000). *J. Appl. Cryst.* **33**, 928–937.
- Malik, A., Sandy, A. R., Lurio, L. B., Stephenson, G. B., Mochrie, S. G. J., McNulty, I. & Sutton, M. (1998). *Phys. Rev. Lett.* **81**, 5832–5835.
- Marty, A., Bessière, M., Bley, F., Calvayrac, Y. & Lefebvre, S. (1990). *Acta Mater.* **38**, 345–350.
- Nicolas, M. & Deschamps, A. (2004). *Metall. Trans. A*, **35**, 1437–1448.
- Perrard, F., Deschamps, A., Bley, F., Donnadiou, P. & Maugis, P. (2006). *Acta Mater.* **39**, 473–482.
- Renaud, G., Lazzari, P., Revenant, C., Barbier, A., Noblet, M., Ulrich, O., Leroy, F., Jupille, J., Borensztein, Y., Henry, C. R., Deville, J. P., Scheurer, F., Mane-Mane, J. & Fruchart, O. (2003). *Science*, **300**, 1416–1419.
- Schlepütz, C., Herger, R., Willmott, P. R., Patterson, B. D., Bunk, O., Brönnimann, C., Heinrich, B., Hülsen, B. & Heikenberry, E. F. (2005). *Acta Cryst.* **A61**, 418–425.
- Schmidbauer, M., Grigoriev, D., Hanke, M., Schäffer, P. & Köhler, R. (2005a). *Phys. Rev. B*, **71**, 115324(1–11).
- Schmidbauer, M., Grigoriev, D., Hanke, M., Schäffer, P. & Köhler, R. (2005b). *Phys. Rev. B*, **71**, 115323(1–8).
- Simon, J.-P., Jousseau, V. & Rolland, G. (2007). *J. Appl. Cryst.* **40**, s363–s366.
- Simon, J.-P. & Lyon, O. (1994). *Resonant Anomalous X-ray Scattering*, edited by G. Materlick, C. J. Spark & K. Fischer, pp. 305–322. The Netherlands: Elsevier Science B.V.
- Spalla, O., Lyonard, S. & Testard, F. (2003). *J. Appl. Cryst.* **36**, 338–347.
- Stadler, L.-M., Sepiol, B., Weinkamer, R., Hartmann, M., Fratzl, P., Kantelhardt, J.-W., Zontone, F., Grübel, G. & Vogl, G. (2004). *Phys. Rev. B*, **68**, 180101(1–4).
- Tatchev, D., Goerigk, G., Valova, E., Dille, J., Kranold, R., Amyanov, S. & Delplancke, J.-L. (2005). *J. Appl. Cryst.* **38**, 787–794.
- Testemale, D., Coulet, M.-V., Hazemann, J.-L., Simon, J.-P., Bley, F., Geyamond, O. & Argoud, R. (2005). *J. Chem. Phys.* **122**, 194505(1–7).
- Vartanyants, I., Robinson, I. K., Onken, J. D., Pfeifer, M. A., Williams, G. J., Pfeiffer, F., Metzger, H., Zhong, Z. & Bauer, G. (2005). *Phys. Rev. B*, **71**, 24302(1–9).
- Wagner, C. (1961). *Z. Electrochem.* **65**, 581–591.
- Wagner, R. & Kampmann, R. (1991). *Homogeneous Second Phase Precipitation: a Comprehensive Treatment*. In *Materials Science and Technology*, Vol. 5, edited by P. Haasen. Weinheim: VCH.
- Weinkamer, R. & Fratzl, P. (2003). *Europhys. Lett.* **61**, 261–267.
- Williams, C. E., May, R. P. & Guinier, A. (1999). *Small Angle Scattering of X-ray and Neutrons*. In *X-characterization of Materials*, Part II, edited by E. Lifshin, pp. 211–254. Weinheim: Wiley-VCH.